

# Effect of gap size on flange face corrosion

Soroosh Hakimian  | Abdel-Hakim Bouzid | Lucas A. Hof

Department of Mechanical Engineering,  
École de technologie supérieure,  
Montreal, Québec, Canada

## Correspondence

Lucas A. Hof, Department of Mechanical Engineering, École de technologie supérieure, 1100, rue Notre-Dame Ouest, Montreal, QC H3C 1K3, Canada.  
Email: [lucas.hof@etsmtl.ca](mailto:lucas.hof@etsmtl.ca)

## Funding information

Natural Sciences and Engineering Research Council of Canada (NSERC), Grant/Award Numbers: RGPIN-2019-05973, RGPIN-2021-03780

## Abstract

Bolted flanged joints play a critical role in offshore wind turbine tower structures, serving as integral components that connect various sections of the tower. This research study employs electrochemical techniques to investigate the effect of gap dimensions, which determine the crevice gap thickness and crevice depth, on corrosion behavior of 321 stainless steel flange sample plates in a 3.5 wt% NaCl solution at 50°C. Gaskets are used in this study to create gaps between two flange surfaces. A novel fixture is utilized to simulate the applied stress on the gasket, fluid flow within the fixture, and the geometric aspects of the gasket and flange. The findings reveal that increasing the gap thickness from 1.58 to 6.35 mm results in a rise in the general corrosion rate of the flange surface from 0.09 to 1.03 mm y<sup>-1</sup>, and crevice corrosion initiation time increases from 0.23 to 3.12 h. Furthermore, reducing the crevice depth ( $d$ ) from 7.49 to 0 mm leads to a decrease in the general corrosion rate from 0.09 mm y<sup>-1</sup> to 0.04 μm y<sup>-1</sup>, and cases with  $d = 3.81$  and  $d = 0$  mm show no observable crevice corrosion after potentiostatic tests.

## KEYWORDS

bolted flanged joints, crevice corrosion, gap size, offshore wind turbine

## 1 | INTRODUCTION

Bolted flanged joints are a type of connection in which two flanges are tightened together with bolts and may include a gasket compressed between them to provide sealing.<sup>[1]</sup> These joints are commonly used in various industrial applications, such as offshore wind turbines (OWTs), pressure vessels, pipeline systems, and other industries for the purpose of connecting sections.<sup>[2,3]</sup> OWTs are generally composed of three primary components: the tower, transition piece (TP), and foundation. The main application of bolted flanged joints in OWTs is for connecting the different tower segments.<sup>[4]</sup> These joints are vulnerable to fatigue corrosion in marine environments due to the combination of strong wind-

wave loads and high corrosivity. It is well established that a direct correlation between corrosion and fatigue failure exists, as corrosion accelerates the initiation and propagation of fatigue cracks.<sup>[5]</sup> The corrosion of bolts in bolted flanged joints has been the subject of a lot of studies in OWT towers.<sup>[6]</sup> However, the initiation and propagation of corrosion at the interface of flanges remain a research gap in the field of corrosion of bolted flanged joints. Gaskets are widely used in bolted flanged connections to provide a tight seal by filling the leak paths and compensating for the unevenness and roughness on the flange surfaces.<sup>[7]</sup> According to reported failure cases in the literature, crevice corrosion initiates on the flange faces due to the presence of occluded areas at the interface of the flange and

This is an open access article under the terms of the [Creative Commons Attribution](https://creativecommons.org/licenses/by/4.0/) License, which permits use, distribution and reproduction in any medium, provided the original work is properly cited.

© 2024 The Authors. *Materials and Corrosion* published by Wiley-VCH GmbH.

gaskets.<sup>[8]</sup> Identifying corrosion at the flange interface before failure is a challenging task. Neglecting this detection may lead to potentially costly consequences.<sup>[9]</sup> Gaps and crevices between flanges, arising from raised faces or the presence of the gasket, joint loosening due to creep-relaxation,<sup>[3,10,11]</sup> rotation on the flange,<sup>[12,13]</sup> and waviness and misalignment,<sup>[14]</sup> represent potential sites for crevice corrosion.

Crevice corrosion is a common failure mode observed in corrosion-resistant alloys (CRAs) and is considered more hazardous than pitting corrosion as it occurs in occluded regions that are generally inaccessible and invisible. Critical factors influencing crevice corrosion include environmental factors, such as pH, temperature, and chloride concentration, the chemical composition and microstructure of the metal, and crevice geometry. While most studies on crevice corrosion focus on the impact of pH, temperature, chloride concentration, and alloying compositions, only a few papers consider the effect of crevice geometry on crevice corrosion.<sup>[15,16]</sup> Additionally, the studied sizes of crevice geometries do not align with the actual sizes present in real-world engineering structures. Crevice geometry encompasses factors, such as crevice gap thickness, depth, and the surface electrode ratio of inside to outside of the crevice, that significantly influence reactions within the crevice, including the concentration of oxygen,  $H^+$ , and  $Cl^-$ .<sup>[17,18]</sup>

Hence, this article aims to utilize a fixture developed by the authors<sup>[19]</sup> for investigating the impact of the gasket geometry on crevice corrosion in bolted flanged joints. The fixture simulates real crevice geometry conditions by applying a range of compression loads similar to those in actual bolted joints in wind turbine and pipeline applications. It also allows the use of gaskets in accordance with ASME B16.5. Flange and gasket sizes and materials are selected based on the most commonly used in bolted flanged joints applications. In addition, the fixture is a sealed container to facilitate the study of corrosion in the presence of fluid flow in a closed loop to mimic an operation of a bolted flanged joint in a piping system. Electrochemical techniques, including cyclic potentiodynamic polarization (CPP), electrochemical impedance spectroscopy (EIS), and potentiostatic tests, are employed to examine the influence of flange and gasket geometry on the initiation and propagation of crevice corrosion.

## 2 | MATERIALS AND METHODS

### 2.1 | Test fixture

The test fixture is the central part of the experimental setup and is representative of a bolted flange joint.

Indeed, this is where the flange platens and gasket are located and wetted by the fluid to allow for corrosion to take place. The corrosion quantification test (COQT) fixture is designed to mimic an ASME B16.5, NPS 2 class 150 gasket according to ASME B16.21 dimensions bolted flanged joint as done with the successful aged relaxation leakage adhesion (ARLA) device<sup>[20,21]</sup> used to measure weight loss, load retention, gasket relaxation, and leakage tightness after aging a sheet gasket material in an oven. Figure 1 shows the COQT test fixture that can assess and quantify corrosion of the flange and gasket material pairs. This figure shows the different parts of the fixture. The central stud allows the application of the compressive load on the gasket through the circular compression plates using a hydraulic tensioner. The compression plates have slots to measure the variation of gasket thickness before and after the corrosion tests by a caliper. In addition, the compression plates have entrance and exit ports for the circulation of the electrolyte. The used flange plates can easily be changed to new ones after each test to study the influence of the different experimental parameters and service conditions. The electrical insulator provides electrical insulation between the sample plates and the compression plates to accurately measure the corrosion of the sample plates and avoid corrosion of the rest of the fixture. A plain washer is used to increase the contact area between the compression plate and the Belleville washer. The Belleville washers are useful to maintain the preload in the assembly and adjust the stiffness of the bolt joint if needed, which is an important parameter when considering relaxation. The load ring or spacer provides a robust contact interface for the Belleville washers. The O-rings prevent electrical contact of the stud with the plates and provide a seal to the outside boundary. The plain washer is used to increase the contact area between the compression plates and the nuts. The volume of the inside chamber is 20 mL. The gasket sizes are within an internal diameter (ID) of 1.31 in. and an outer diameter (OD) of 2.95 in. with thicknesses ranging from 1/16 to 1/4 in. A full Wheatstone strain gauge bridge is installed on the central stud (transducer in mV) to measure the force of the central stud. This force measurement can subsequently be converted into the average gasket contact stress by simply dividing the force by the gasket area.

### 2.2 | Test rig

The COQT fixture is part of the test rig shown in Figure 2. It is connected to a tubing circuit of the electrolyte that has different equipment and

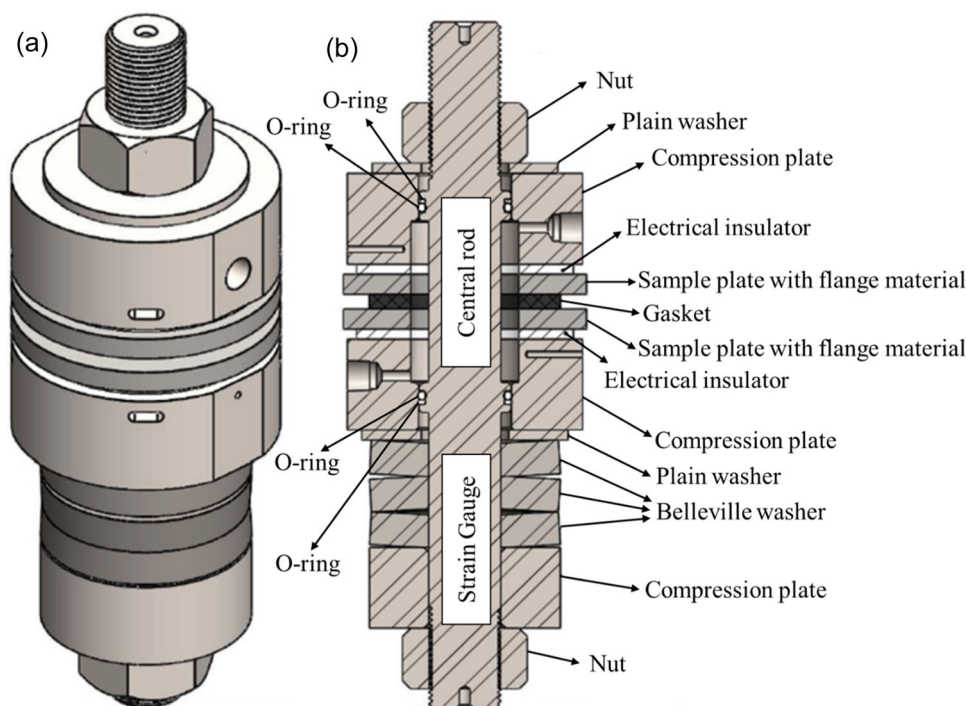


**FIGURE 1** Test fixture: (a) 3D view and (b) cross-section view and labeling of each item (adapted from reference<sup>[19]</sup>). [Color figure can be viewed at [wileyonlinelibrary.com](https://onlinelibrary.wiley.com)]

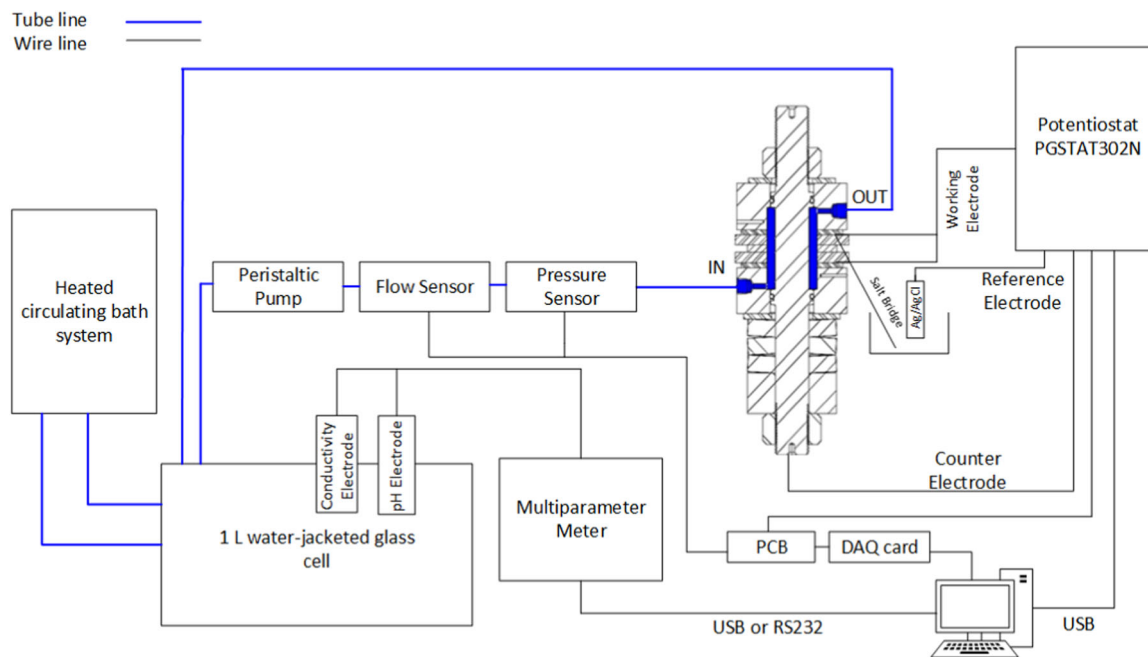


**FIGURE 2** Schematic of the test rig including: pH and conductivity meter; pH electrode; conductivity electrode; thermostatic water bath; peristaltic pump; flow sensor; pressure sensor; working electrode connection; counter electrode connection; reference electrode; salt bridge; PCB; DAQ card; PC (adapted from reference<sup>[19]</sup>). [Color figure can be viewed at [wileyonlinelibrary.com](https://onlinelibrary.wiley.com)]

instrumentation. The multiparameter meter (Thermo-Fisher STARA2150 series) simultaneously measures the pH, conductivity, and temperature of the electrolyte through the conductivity electrode and pH

electrode. The water-jacketed glass cell is a type of apparatus used to control and maintain the temperature ( $\pm 0.1^\circ\text{C}$ ) of the test solution. The glass cell is surrounded by a jacket filled with water. This water

jacket acts as a temperature buffer and helps maintain a stable temperature within the cell. The peristaltic pump (BRL Life Technologies CP-600) provides continuous solution flow from the water-jacketed glass cell to the test fixture. The flow sensor and pressure transducer continuously monitor the flow and pressure of the solution. The three-electrode cell, used for electrochemical measurements, includes the sample flange plates (321 SS) as a working electrode (W.E.), a saturated Ag/AgCl as a reference electrode (R.E.), and the 316 L SS central stud as a counter electrode (C.E.). All measured potentials are done with respect to the Ag/AgCl electrode. An Autolab potentio/galvanostat, PGSTAT302N-High Performance, is used to produce the polarization curves for the discussed potential ranges. Nova software version 2.1.7 is used for analyzing electrochemical data. A salt bridge is used as a connection between the solution in the test fixture and the reference electrode to minimize the ohmic drop contribution between the reference and working electrodes. As indicated in Figure 2, the solution flows in and out from the bottom to the top of the fixture; hence, all the inner parts, including the gasket and the metallic sample plates, are soaked with the solution.

The analog signals from the sensors are transmitted to the printed circuit board (PCB) and converted to numerical values by a National Instruments data acquisition card (DAQ). The DAQ, potentiostat, and multiparameter meter

are connected directly to the computer through a USB connection. The heated circulating bath system circulates water within the jacket of the glass cell and controls the temperature through a heating or cooling system.

### 2.3 | Materials

The sample plates have an OD of 2.95 in. (74.93 mm), an ID of 1.31 in. (33.27 mm), and a thickness of 0.25 in. (6.35 mm) (as shown in Figure 3a). The material of the sample plate is 321 stainless steel (SS), with a chemical composition according to the ASTM A182 standard specification for SS flanges. The chemical composition is provided in Table 1. Virgin polytetrafluoroethylene gaskets of various sizes are used between the sample plates, following the specifications of ASME B16.21 for non-metallic flat gaskets used in flanges. This approach is aimed at investigating the influence of gasket sizes (thickness and ID) on the corrosion behavior of flange faces by creating different crevice gap thickness and crevice depth. The exposed area to the solution on the flange sample plate is determined by the gasket ID used between two sample plates, illustrated in Figure 3b.

Equation (1) presents the relation for calculating the exposed surface area on the flange face. In this equation,  $ID_g$  represents the gasket ID in cm, and  $ID_f$  denotes the flange ID in cm.

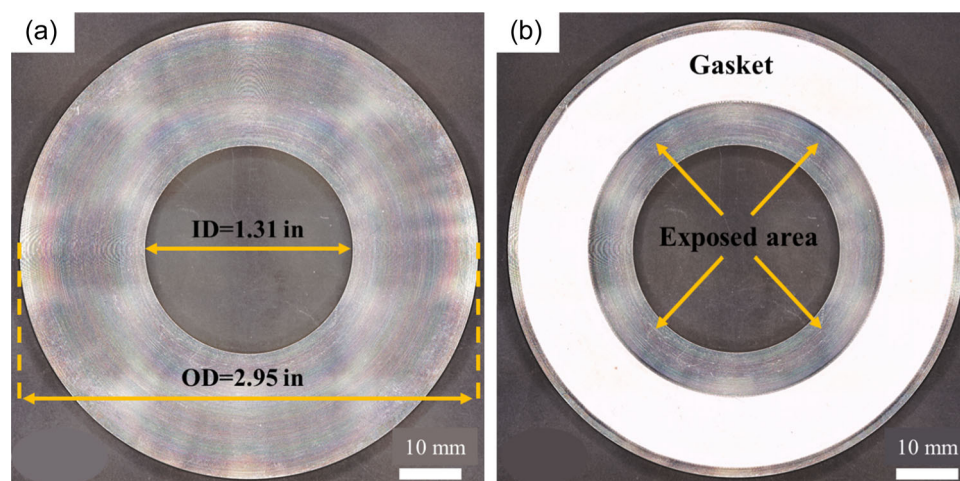


FIGURE 3 The sample plate used in the joint; (a) the inner diameter (ID) and outer diameter (OD) of the sample plate; (b) the exposed surface area to the solution for the gasket with the ID of 48.26 mm. [Color figure can be viewed at [wileyonlinelibrary.com](http://wileyonlinelibrary.com)]

TABLE 1 Chemical composition of 321 SS sample plate (wt%).

C	N	Si	P	S	Cr	Mn	Ni	Mo	Cu	Ti
0.049	0.024	0.54	0.03	0.001	17.45	1.57	9	0.37	0.48	0.53

Exposed surface area on the flange face

$$= \left( ID_g^2 - ID_f^2 \right) \times \frac{\pi}{4}. \quad (1)$$

This study employs gasket thicknesses as typically utilized in bolted flange joints: 1/16 in. (1.58 mm), 1/8 in. (3.17 mm), and 1/4 in. (6.35 mm). The gasket IDs are chosen based on the gasket groups specified in the ASME B16.21 standard. Two types of gaskets are considered: the first type, known as a full-face gasket that, covers the entire flange face. In the second type, the gasket ID equals the outer diameter of the pipe, implying that the exposed area on the flange face is equivalent to the pipe thickness. Pipe schedule describes the wall thickness of a pipe, with common schedule number being 40. According to ASME B36, the thickness for pipes with schedules 40 and nominal pipe sizes of 2 and 8 is 0.15 in. (3.81 mm) and 0.3 in. (7.49 mm), respectively. Consequently, three distinct values for the gasket ID are selected: 1.31 in. (33.27 mm), 1.61 in. (40.89 mm), and 1.91 in. (48.26 mm).

When considering gasket sizes in this study, two variables are defined: gasket thickness or crevice gap thickness, denoted by  $g$ , representing the gap between two flange sample plates; and the distance  $d$  between the flange ID and the gasket ID (crevice depth), obtained from Equation (2). Here,  $ID_g$  and  $ID_f$  represent the gasket ID and the flange ID in mm, respectively.

$$d = (ID_g - ID_f) \div 2. \quad (2)$$

The configuration of the flange and gasket is depicted in Figure 4. Figure 4a presents the cross-section of an actual bolted flanged joint with a full-face gasket that entirely covers the flange face, and it identifies all the components of a bolted flanged joint. Figure 4b,c illustrates bolted flanged joints with gaskets having IDs larger than the flange ID, with the variables  $d$  and  $g$  represented by yellow arrows. Figure 4d–f demonstrates how the configuration of the flange sample plate and gasket in the experiments of this study replicates the

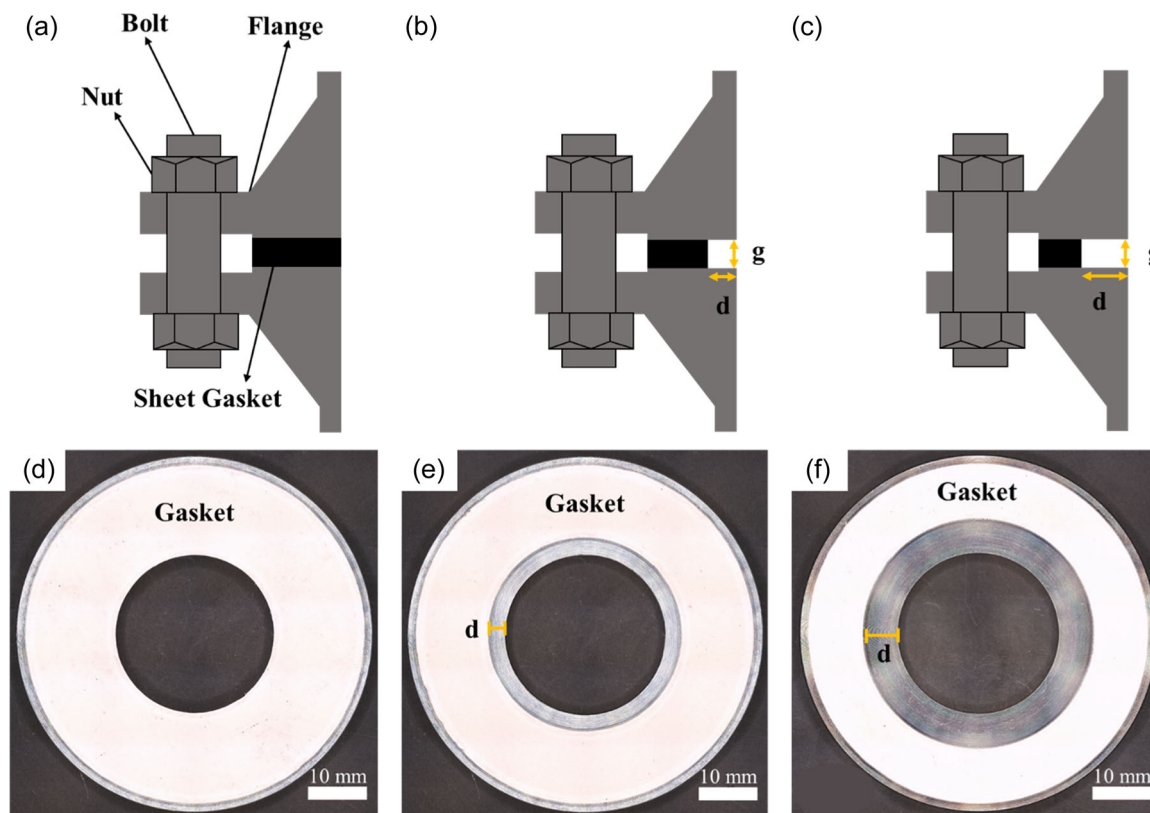


**FIGURE 4** Configuration of the flange and gasket in a real bolted flanged gasket joint: (a) schematic cross-section illustrating the bolted flanged joint with a full-face gasket, including component identification; (b) schematic cross-section of the bolted flanged joint with a gasket featuring an ID of 36.05 mm, with yellow arrows indicating variables  $d$  and  $g$ ; (c) schematic cross-section of the bolted flanged joint with a gasket having an ID of 48.26 mm, with yellow arrows indicating variables  $d$  and  $g$ ; (d) image depicting the sample plate and gasket with an ID of 33.27 mm; (e) image showing the sample plate and gasket with an ID of 36.05 mm; (f) image illustrating the sample plate and gasket with an ID of 48.26 mm. ID, inner diameter. [Color figure can be viewed at [wileyonlinelibrary.com](https://onlinelibrary.wiley.com)]

TABLE 2 The dimensions of the gasket used in the joint for experiments.

Gasket No.	Gap thickness/g (mm)	ID (mm)	OD (mm)	Weight (g)	Depth/d (mm)	Exposed surface area on the flange (cm <sup>2</sup> )
1	1.58	48.26	71.12	9.25	7.49	9.73
2	3.17	48.26	71.12	19.28	7.49	9.73
3	6.35	48.26	71.12	38.95	7.49	9.73
4	1.58	40.89	71.12	11.37	3.81	4.38
5	1.58	33.27	71.12	13.51	0	–

Abbreviations: ID, inner diameter; OD, outer diameter.

actual flange and gasket configuration in real-world bolted flanged gasket joints.

Concluding this section, Table 2 summarizes the dimensions of the gaskets utilized in this study, along with key variables, where  $d$  is crevice depth calculated using Equation (2), and  $g$  represents the crevice gap thickness measured with a caliper. Each configuration of gasket and flange sample plate is assigned a Gasket No. as an identifier, and this number will be used throughout the rest of the article, as indicated in Table 2. For Gasket No. 5, both the exposed surface area on the flange face and the  $d$  value are 0, as the ID of the gasket matches the ID of the flange sample plate, in accordance with Equations (1) and (2).

## 2.4 | Corrosion characterization

To understand the corrosion mechanism occurring on the surfaces of the flanges in bolted flanged joints, the current study employs electrochemical techniques and microscopic characterization methods. These techniques will be discussed in the following sections.

### 2.4.1 | Electrochemical measurements

Before starting the electrochemical measurements, the fixture shown in Figure 1 is mounted on a stand equipped with a hydraulic tensioner to compress the gasket to an average initial stress of 15 MPa. The water-jacketed glass cell is filled with a 3.5 wt% NaCl solution (distilled water and analytical grade of NaCl) and the solution is heated to 50°C. The peristaltic pump circulates the solution in the fixture with a flow rate of 90 mL/min. The sample plates are degreased by ethanol in ultrasonic for 20 min, and then air dried before electrochemical tests.

The EIS test is initiated 6 h after the solution has been in circulation inside the fixture, allowing sufficient time

for the surfaces of the samples and the interface between the gasket and sample plates to become wet and for the open circuit potential (OCP) to stabilize. This EIS test is performed at the OCP over a frequency range of 10 000–0.01 Hz with a sinusoidal alternating amplitude of 50 mV.

The CPP is the most common technique for measuring critical crevice corrosion potentials. This method is outlined in ASTM G61,<sup>[22]</sup> and it identifies the potential at which crevice corrosion initiates ( $E_{\text{crev}}$  or  $E_b$ ), the repassivation potential ( $E_{\text{rep}}$ ), and the corrosion potential ( $E_{\text{corr}}$ ). The scan begins from  $-0.05$  V versus OCP and continues until the current reaches 5 mA, at which point it is reversed. The scan is discontinued when the potential reaches  $-0.05$  V or the backward scan current density intersects the forward scan current density. For both forward and reverse scans, the scan rate equals 0.0167 mV/s. The exposed surface area of the 321 SS sample plates varies according to Table 2. To calculate the current density, the current values obtained from the polarization tests are divided by the corroded area obtained from microscopic characterization, as explained in Section 2.4.2. To calculate the general corrosion rate (CR) of the 321 SS sample plates with different Gasket No., the obtained corrosion current densities ( $i_{\text{corr}}$ ) from the CPP curves are used in Equation (3). This equation converts the corrosion current density to the corrosion rate.<sup>[23]</sup>

$$\text{CR} = K \frac{i_{\text{corr}}}{\rho} \text{EW}, \quad (3)$$

where CR represents the corrosion rate in mm/y,  $i_{\text{corr}}$  signifies the corrosion current density in  $\mu\text{A}/\text{cm}^2$ ,  $\rho$  represents the density in  $\text{g}/\text{cm}^3$ , and  $K$  is a constant equal to  $3.27 \times 10^{-3}$  mm/g/ $\mu\text{A}/\text{cm}/\text{year}$ . EW is the dimensionless equivalent weight and denotes the mass of metal oxidized by the passage of 1 Faraday (96 500 C) of electric charge. The values of EW and  $\rho$  for 321 SS are

provided in ASTM G102 and ASTM G1,<sup>[23,24]</sup> and they are defined as 25.13 and 7.94 g/cm<sup>3</sup>, respectively.

Crevice corrosion initiation and propagation are assessed in a 3.5 wt% NaCl solution at 50°C through potentiostatic polarization using the same rig and fixture as the one for cyclic potentiodynamic polarization. The hold potential is determined before the transpassive dissolution of 321 SS or the potential leading to active metal dissolution. This potential is chosen based on the CPP curves, and the selected potential is 0.15 V.

## 2.4.2 | Surface characterization

The corroded area of each flange sample plate is measured after CPP and potentiostatic polarization. The images of the corroded area are obtained using a Keyence VHX-7000 digital microscope. Then the area of the corroded surface is measured by ImageJ software.<sup>[25]</sup> The entire corroded surface area ( $A_c$ ) is calculated using Equation (4).

$$A_c = \sum_i^n A_{c,i}, \quad (4)$$

where  $A_{c,i}$  represents the corroded area in region  $i$  and  $n$  stands for the number of observed corroded areas on the sample plate surface. The morphology of the corroded surface on the flange face is examined by scanning electron microscopy (SEM).

## 3 | RESULTS

The results section is divided into four parts: (1) CPP curves, (2) crevice corrosion initiation and propagation, (3) general corrosion resistance, and (4) corrosion morphology. All of these results are obtained under the same testing conditions, including temperature, fluid flow rate, and average gasket contact stress, as mentioned in Section 2.4.1.

### 3.1 | CPP curves

The polarization curves, depicted in Figure 5, illustrate the corrosion potential ( $E_{\text{corr}}$ ) and breakdown potential ( $E_b$ ) used for assessing the corrosion behavior of the sample plates. The corrosion potential represents the potential of the working electrode (sample plate) against the reference electrode when no potential or current is applied to the working electrode. This parameter serves as a thermodynamic indicator, reflecting the tendency of the working electrode to undergo corrosion reactions

under specific conditions. The  $E_b$  is characterized by a significant and rapid increase in current density. A higher positive  $E_b$ , achieved at a constant scan rate in the polarization curve, suggests a reduced susceptibility of the sample plate to the initiation of localized corrosion, such as crevice or pitting corrosion.<sup>[15,26]</sup>

The potential difference  $|E_{\text{corr}} - E_b|$  signifies the inclination toward localized corrosion, with higher values indicating a diminished tendency.<sup>[27]</sup> Due to the simultaneous passivation in the anodic branch of the polarization curves, the anodic Tafel region is not well-defined. Therefore, to determine the general corrosion rate of the flange sample plates, the  $i_{\text{corr}}$  is calculated by intersecting the extrapolation of the cathodic branch at  $E_{\text{corr}}$ .<sup>[28]</sup> Table 3 provides an overview of the key electrochemical parameters derived from the polarization curves in Figure 5. The polarization curves presented in Figure 5a–e all demonstrate positive hysteresis in the CPP curve, where the reverse scan current density surpasses that of the forward scan. This positive hysteresis serves as an indicator of the initiation of localized corrosion.<sup>[29]</sup> Notably, in Figure 5c, the backward scan intersects with the forward scan, indicating repassivation at that specific potential, also known as  $E_{\text{rep}}$ .<sup>[30]</sup> The more positive the  $E_{\text{rep}}$ , the less likely localized corrosion occurs.<sup>[22]</sup> It is essential to highlight that  $E_{\text{rep}}$  has a potential higher than  $E_{\text{corr}}$  for the sample plate used with Gasket No. 3, signifying that at  $E_{\text{corr}}$ , localized corrosion does not occur. Localized corrosion occurs if the corrosion potential of a metal in a given environment exceeds the  $E_{\text{rep}}$ .<sup>[31]</sup> The  $E_{\text{corr}}$  values are  $-0.01$ ,  $0.05$ ,  $-0.15$ ,  $-0.05$ , and  $-0.06$  V for the tests with Gasket Nos. 1, 2, 3, 4, and 5, respectively. The  $E_b$  values are  $0.17$ ,  $0.18$ ,  $-0.03$ ,  $0.13$ , and  $0.17$  V for test with Gasket Nos. 1, 2, 3, 4, and 5, respectively. Among the  $|E_{\text{corr}} - E_b|$  values, the highest value is observed for the tests with Gasket No. 5, which was found to be  $0.23$  V. The remaining values are ranked in the following order: Gasket Nos. 1 and 4, both of which are  $0.18$  V; Gasket No. 2, which is  $0.13$  V; and Gasket No.3, which is  $0.12$  V. The corrosion rates for tests with Gasket No. 1, Gasket No. 2, and Gasket No. 3 are  $0.09$ ,  $0.4$ , and  $1.03$  mm y<sup>-1</sup>, respectively. These results suggest that as the gap thickness increases, the corrosion rate also increases. Conversely, for the test with Gasket No. 4, the corrosion rate is  $0.03$  mm y<sup>-1</sup>, and for the test with Gasket No. 5, it is  $4.17\text{e}-04$  mm y<sup>-1</sup>, indicating a decrease in corrosion rate with a reduction in the  $d$  (crevice depth) value.

According to the polarization curves, at  $E_b$ , rapid and continuous increase of current is observed which is related to the localized corrosion. To study localized corrosion on the flange sample plates with different gasket sizes, the top view and microscopic images of the corroded samples are shown in Figure 6. As

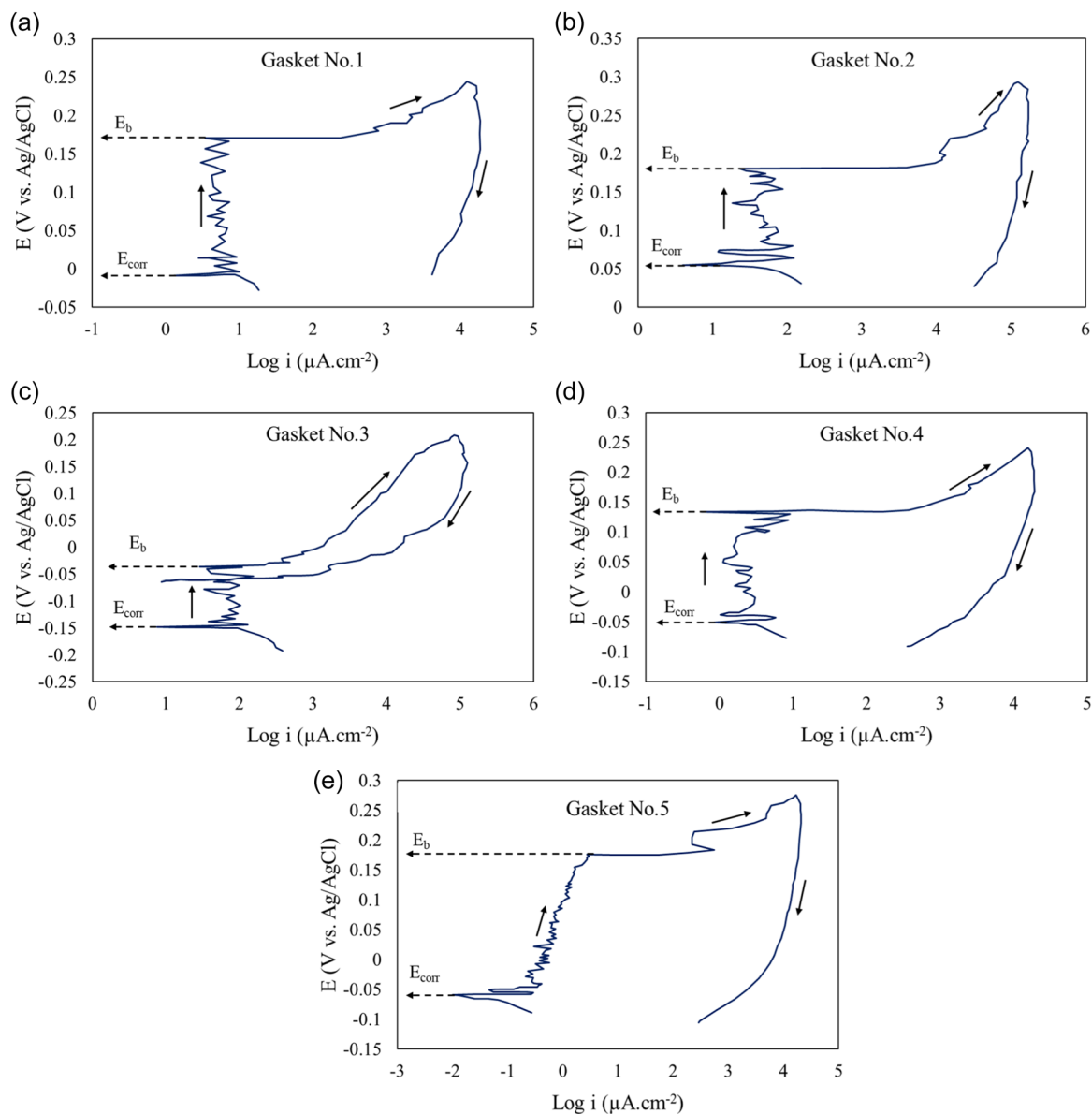


FIGURE 5 Cyclic potentiodynamic polarization curves of 321 SS sample plates in 3.5 wt% NaCl at 50°C for tests with different gasket sizes; (a) Gasket No. 1; (b) Gasket No. 2; (c) Gasket No. 3; (d) Gasket No. 4; and (e) Gasket No. 5. [Color figure can be viewed at [wileyonlinelibrary.com](https://onlinelibrary.wiley.com/doi/10.1002/maco.202414367)]

TABLE 3 Electrochemical parameters obtained from the CPP curves.

Gasket No.	$E_{\text{corr}}$ (V)	$E_b$ (V)	$ E_{\text{corr}} - E_b $ (V)	$i_{\text{corr}}$ ( $\mu\text{A}\cdot\text{cm}^{-2}$ )	Corrosion rate ( $\text{mm}\cdot\text{y}^{-1}$ )
1	-0.01	0.17	0.18	9.33	0.09
2	0.05	0.18	0.13	38.71	0.4
3	-0.15	-0.03	0.12	99.6	1.03
4	-0.05	0.13	0.18	2.75	0.03
5	-0.06	0.17	0.23	0.04	4.17e-04

Abbreviation: CPP, cyclic potentiodynamic polarization.

**FIGURE 6** Corroded flange sample plates after CPP test: (a) Top view of the sample plate with Gasket No. 1; (b) top view of the sample plate with Gasket No. 2; (c) top view of the sample plate with Gasket No. 3; (d) top view of the sample plate with Gasket No. 4; (e) top view of the sample plate with Gasket No. 5; (f) Microscopic image of the corroded area for the sample plate Gasket No. 1; (g) microscopic image of the corroded area for the sample plate with Gasket No. 2; (h) microscopic image of the corroded area for the sample plate with Gasket No. 3; (i) microscopic image of the corroded area for the sample plate Gasket No. 4; and (j) microscopic image of the corroded area for the sample plate with Gasket No. 5. CPP, cyclic potentiodynamic polarization. [Color figure can be viewed at [wileyonlinelibrary.com](https://onlinelibrary.wiley.com)]

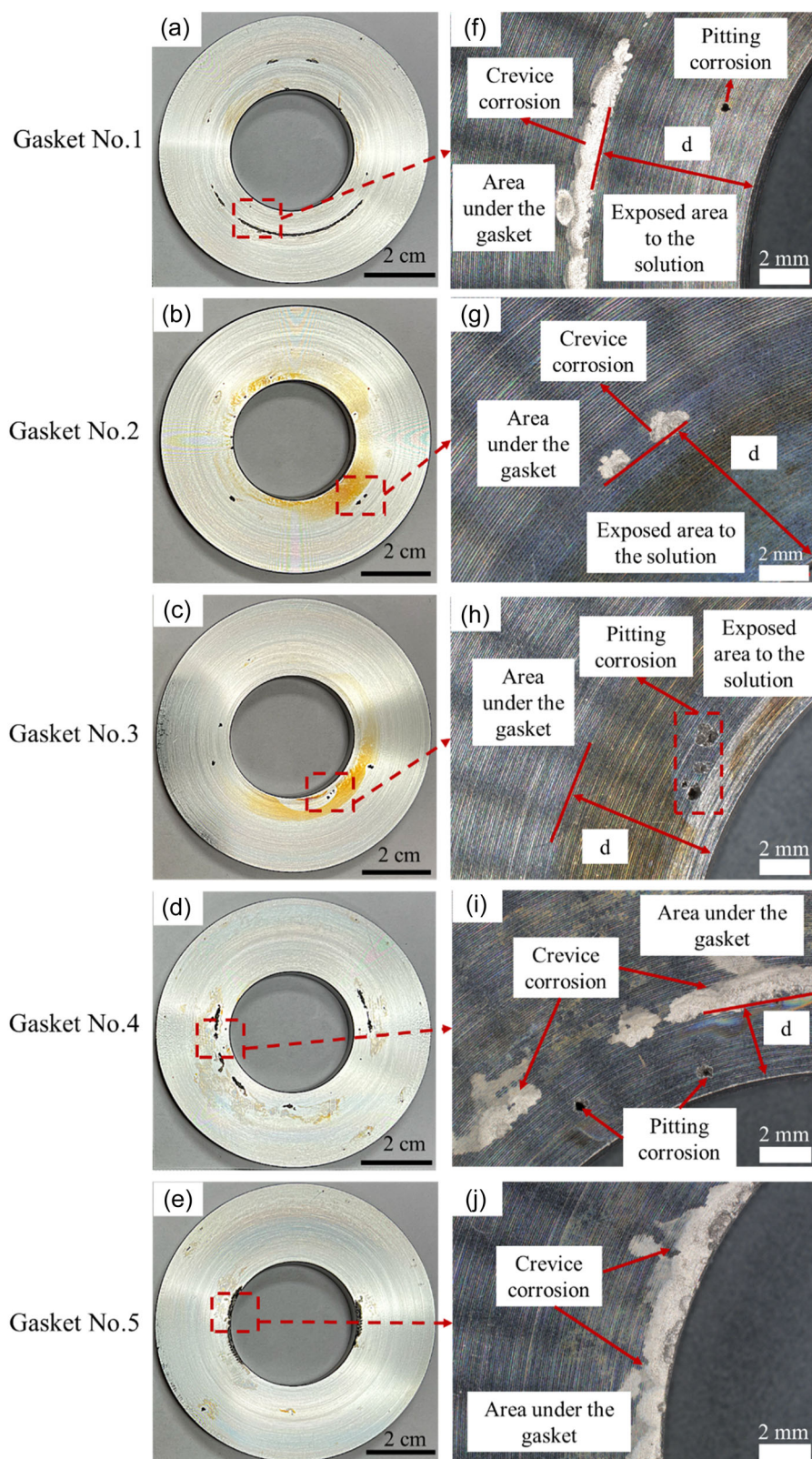


TABLE 4 Characteristics of crevice and pitting corrosion obtained through examination of the corroded surfaces.

Gasket No.	Depth/ <i>d</i> (mm)	Gap thickness/ <i>g</i> (mm)	Crevice corrosion area (cm <sup>2</sup> )	Maximum crevice depth	Number of pits	Maximum pit depth (μm)	Average pit depth (μm)
1	7.49	1.58	0.4	218.1	4	703.7	462.7
2	7.49	3.17	0.04	478.2	6	704.4	528.6
3	7.49	6.35	0	0	7	903.8	661.3
4	3.81	1.58	0.34	311.4	7	657.5	429.5
5	0	1.58	0.28	661.6	0	0	0

shown in Figure 6a, both crevice corrosion and pitting corrosion occurred on the sample plate used with Gasket No. 1. The magnified image of (a) is shown in Figure 6f, which shows that crevice corrosion significantly occurred in the interface of the gasket with the sample plate or the boundary between the area under the gasket and the area exposed to the solution. However, pitting corrosion occurred in the area exposed to the solution. For the sample plate with Gasket No. 2 (Figure 6b), both crevice and pitting corrosion are observed on the flange sample plate; however, the magnified image (Figure 6g) shows that the crevice corrosion area seems smaller than the crevice corrosion area on the sample plate used with Gasket No. 1. Figure 6c indicates that only pitting corrosion occurred on the flange sample plate, and crevice corrosion is not observed in the interface of the flange and gasket. As shown in Figure 6h, stable pits are formed in the area exposed to the solution. On the flange sample plate with Gasket No. 4 (Figure 6d), both pitting and crevice corrosion are observed on the corroded surface. The magnified image Figure 6i shows that crevice corrosion occurred in the boundary of the area under the gasket and the exposed area to the solution. Figure 6e reveals that for the sample plate used with Gasket No. 5, only crevice corrosion occurred on the flange surface, and the magnified image (Figure 6j) verifies that crevice corrosion started on the flange surface from the interface of the flange and gasket both of which have the same ID.

To assess crevice and pitting corrosion on the flange sample plates, measurements of crevice corrosion area, maximum crevice depth, number of pits, maximum pit depth, and average pit depth are conducted using a Keyence digital microscope at 500× magnification, as reported in Table 4. The results indicate that increasing the gap thickness from 1.58 to 6.35 mm leads to a decrease in crevice corrosion area from 0.4 to 0 cm<sup>2</sup>. Furthermore, the average pit depth increases from 462.7 to 661.3 μm as the gap thickness increases. As *d*

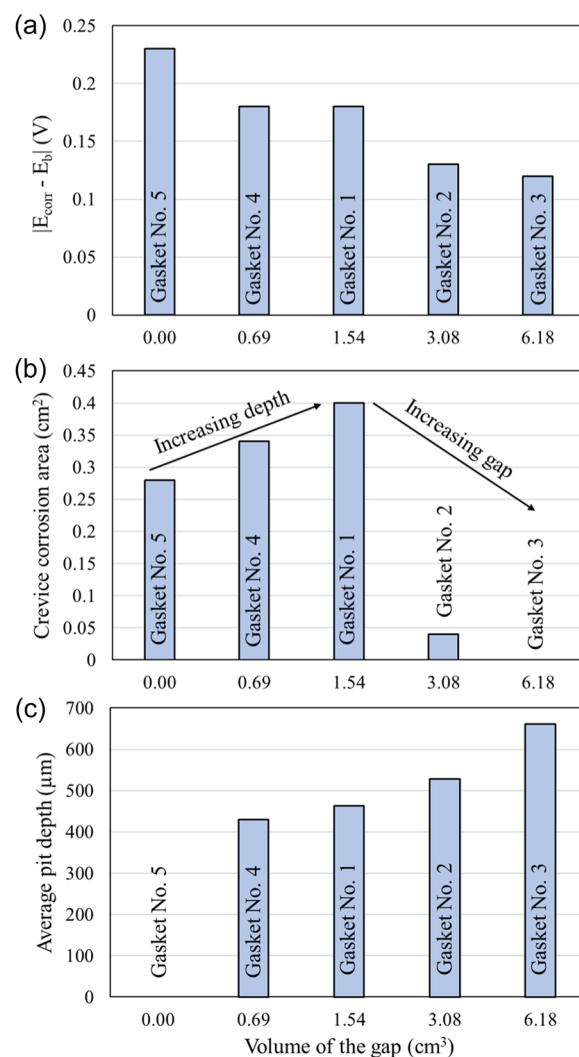
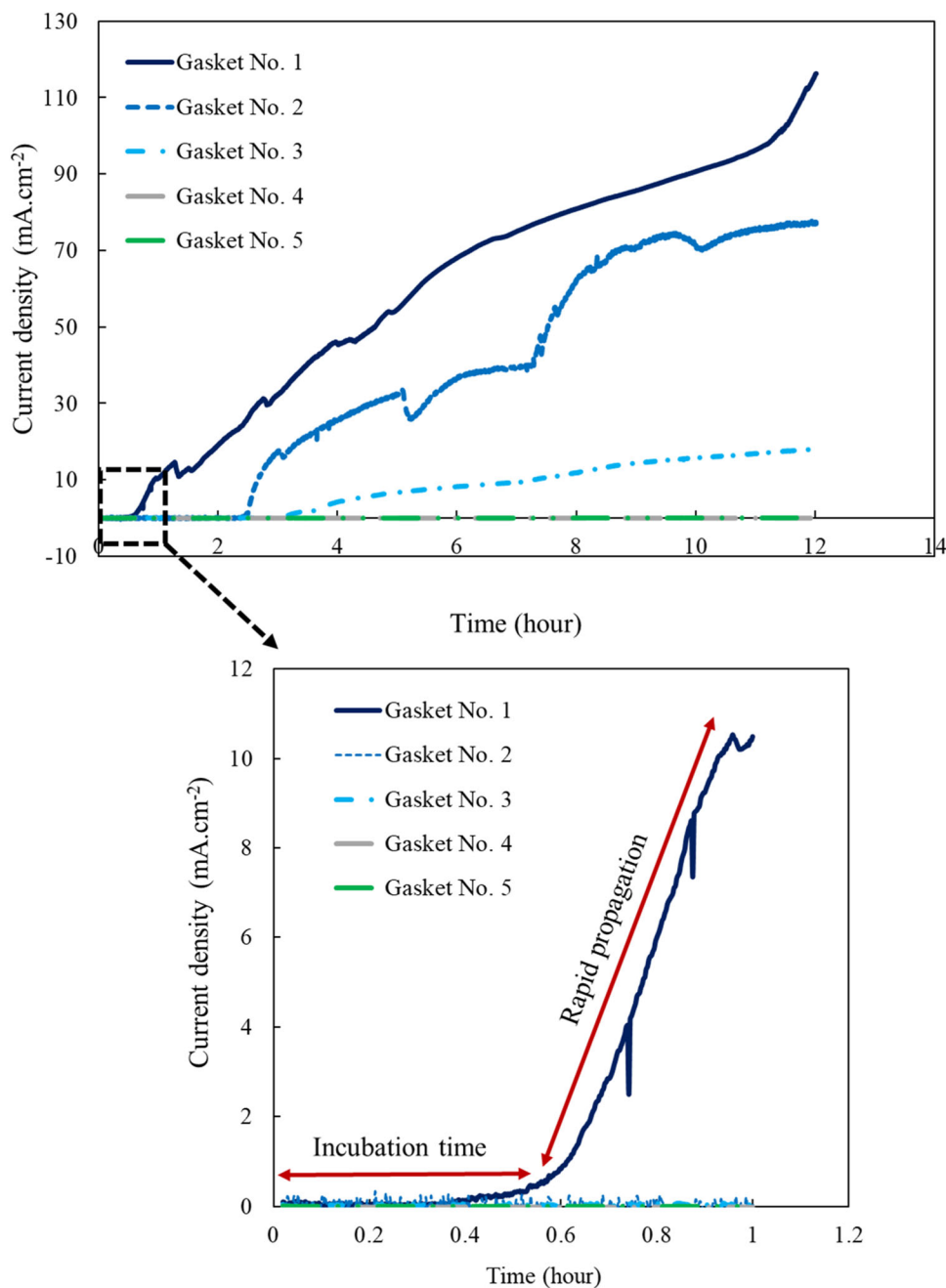


FIGURE 7 Variations in (a) potential range of passive region, (b) crevice corrosion area, and (c) average pit depth versus volume of the gap. [Color figure can be viewed at [wileyonlinelibrary.com](https://onlinelibrary.wiley.com/terms-and-conditions)] [Color figure can be viewed at [wileyonlinelibrary.com](https://onlinelibrary.wiley.com/terms-and-conditions)]

(crevice depth) decreases, both crevice corrosion area and average pit depth decrease. Conversely, the average pit depth decreases from 462.7 at *d* = 7.49 to 429.5 at *d* = 3.81 and becomes 0 at *d* = 0.



**FIGURE 8** Current density versus time curves for different gasket sizes in 3.5 wt% NaCl solution at 50°C for 12 h. The onset, depicted by the dotted line rectangle, magnifies the curve over 1 h of the potentiostatic test. [Color figure can be viewed at [wileyonlinelibrary.com](https://onlinelibrary.wiley.com/doi/10.1002/maco.202414367)]

The information obtained from the CPP tests is presented in the graphs depicted in Figure 7. These graphs illustrate the variations of the passive potential range (Figure 7a), crevice corrosion area (Figure 7b), and average pit depth (Figure 7c) in relation to the gap volume. The gap volume is calculated using Equation (5), with the Gap volume in  $\text{cm}^3$ , exposed surface area on the flange in  $\text{cm}^2$ , and the gap thickness in cm, as per the dimensions provided in Table 2.

$$\text{Gap volume} = \text{Exposed surface area on the flange} \times \text{gap.} \quad (5)$$

Figure 7a reveals that the passive potential range ( $|E_{\text{corr}} - E_b|$ ) decreases with an increase in gap volume. This decrease suggests a breakdown in the passive layer at lower potentials. As all the CPP tests in the forward scan continue until reaching a 5 mA current, samples with a lower passive range exhibit higher average pit

depths (Figure 7c). In the case of Gasket No. 5, which has the highest passive range, the resulting current after breakdown is only derived from the crevice corroded area (Figure 7b). Conversely, in Gasket No. 3, the resulting current only originates from the pitting corrosion formed on the flange surface.

### 3.2 | Crevice corrosion initiation and propagation

The potential for potentiostatic polarization is adjusted to fall within the passivation region, as indicated by the polarization curves in Figure 5. Figure 8a illustrates potentiostatic polarization curves of 321 SS plates in a 3.5% NaCl solution using different gasket sizes over a 12-h period. The information obtained from the potentiostatic curves is presented in Table 5. The crevice corrosion process is divided into two stages based on the polarization curve features, including incubation and propagation. The incubation time represents the duration required for the development of an acidic solution within the crevice. Subsequently, due to a sharp decrease in pH and an increase in  $\text{Cl}^-$  concentration, crevice corrosion propagates spontaneously.<sup>[32]</sup> Table 5 represents data related to both initiation and propagation of crevice corrosion by reporting the initiation time ( $t_{\text{ini}}$ ) and the maximum propagation current density ( $i_{\text{max}}$ ). According to the obtained experimental results, the incubation time for crevice corrosion in the joint increases with an increase of the gap thickness (at a fixed value of  $d$ ). The incubation time for the gasket with a thickness of 1.58 mm is 0.23 h; subsequently, it increases to 2.37 h with a gap thickness of 3.17 mm, and reaching a maximum of 3.12 h when using a gasket with a thickness of 6.35 mm in the joint. Crevice corrosion propagates with the maximum current density of  $116.24 \text{ mA cm}^{-2}$  in 12 h when the gap thickness size is 1.58 mm. The maximum current density decreases to 77.15 and  $18.03 \text{ mA cm}^{-2}$  with an increase of the gap thickness to 3.17 and 6.35 mm,

TABLE 5 Crevice corrosion initiation time and the maximum current density obtained from the potentiostatic polarization test.

Gasket No.	Gap thickness/g (mm)	Depth/d (mm)	$t_{\text{ini}}$ (h)	$i_{\text{max}}$ ( $\text{mA cm}^{-2}$ )
1	1.58	7.49	0.23	116.24
2	3.17	7.49	2.37	77.15
3	6.35	7.49	3.12	18.03
4	1.58	3.81	–	0.06
5	1.58	0	–	0.001

respectively. By decreasing  $d$  from 7.49 to 3.81 and 0 mm (at a fixed value of  $g$ ), there is no significant increase in the current density observed in the potentiostatic curves. The maximum current density for  $d = 3.81$  reaches  $0.06 \text{ mA cm}^{-2}$ , and for  $d = 0$ , it is  $1 \mu\text{A cm}^{-2}$ . These results indicate that increasing the gap thickness leads to damage to the passive layer due to the erosive effect of the flowing solution from inside the fixture. This makes it less aggressive for crevice corrosion to occur. Conversely, reducing the crevice depth, as the gasket shields the flange surface from  $\text{Cl}^-$  ions and the erosive effect of the flowing solution, reveals a wider potential range for passivation.

### 3.3 | General corrosion resistance

To study the effect of gasket size on the general corrosion resistance of the 321 SS flange sample plates, EIS measurements are performed on the sample plates used with different gap thicknesses. In EIS analysis, only tests with the same exposed surface area are considered (Gasket Nos. 1–3). Figure 9a–c shows the EIS Nyquist and Bode plots for different gap thicknesses. It can be observed in the Nyquist plots (Figure 9a) that all spectra exhibit an incomplete capacitive semi-circle, which implies a similar corrosion mechanism for various gap thicknesses. Two time constants are observed in the Bode plots (Figure 9b). Therefore, a two-time-constant electrical equivalent circuit (EEC) inside of Figure 9a is used in the modeling procedure. In the EEC,  $R_s$  denotes the resistance of the solution (electrolyte), with the higher-frequency section of the spectrum linked to the behavior of the electrochemical double-layer capacitance ( $\text{CPE}_1$ ) and charge-transfer resistance ( $R_1$ ). Moving charged species through the passive oxide layer is a slow process, and the low-frequency responses are attributed to these slow processes, characterized by  $\text{CPE}_2$  and  $R_2$ . Instead of using only a pure capacitance ( $C$ ) in the fitting procedure, a frequency-dependent constant phase element,  $\text{CPE} (\Omega^{-1} \text{S}^n \text{cm}^{-2})$  with exponent  $n$ , is employed to achieve a more accurate alignment between theoretical and experimental data. Due to the surface inhomogeneity of the sample, a  $\text{CPE}$  is considered instead of  $C$ .<sup>[33]</sup> EEC parameter values obtained by fitting of the experimental data in Figure 9 are presented in Table 6. Other than the defined parameters, this table includes the total resistance values that are obtained from Equation (6). The  $R_{\text{total}}$  represents the corrosion resistance in  $\text{k}\Omega \text{ cm}^2$ .

$$R_{\text{total}} = R_1 + R_2. \quad (6)$$

According to Table 6, the total corrosion resistance is  $10\,725 \text{ k}\Omega \text{ cm}^2$  when the gap thickness is 1.58 mm, and then it decreases to  $482 \text{ k}\Omega \text{ cm}^2$  by increasing the gap

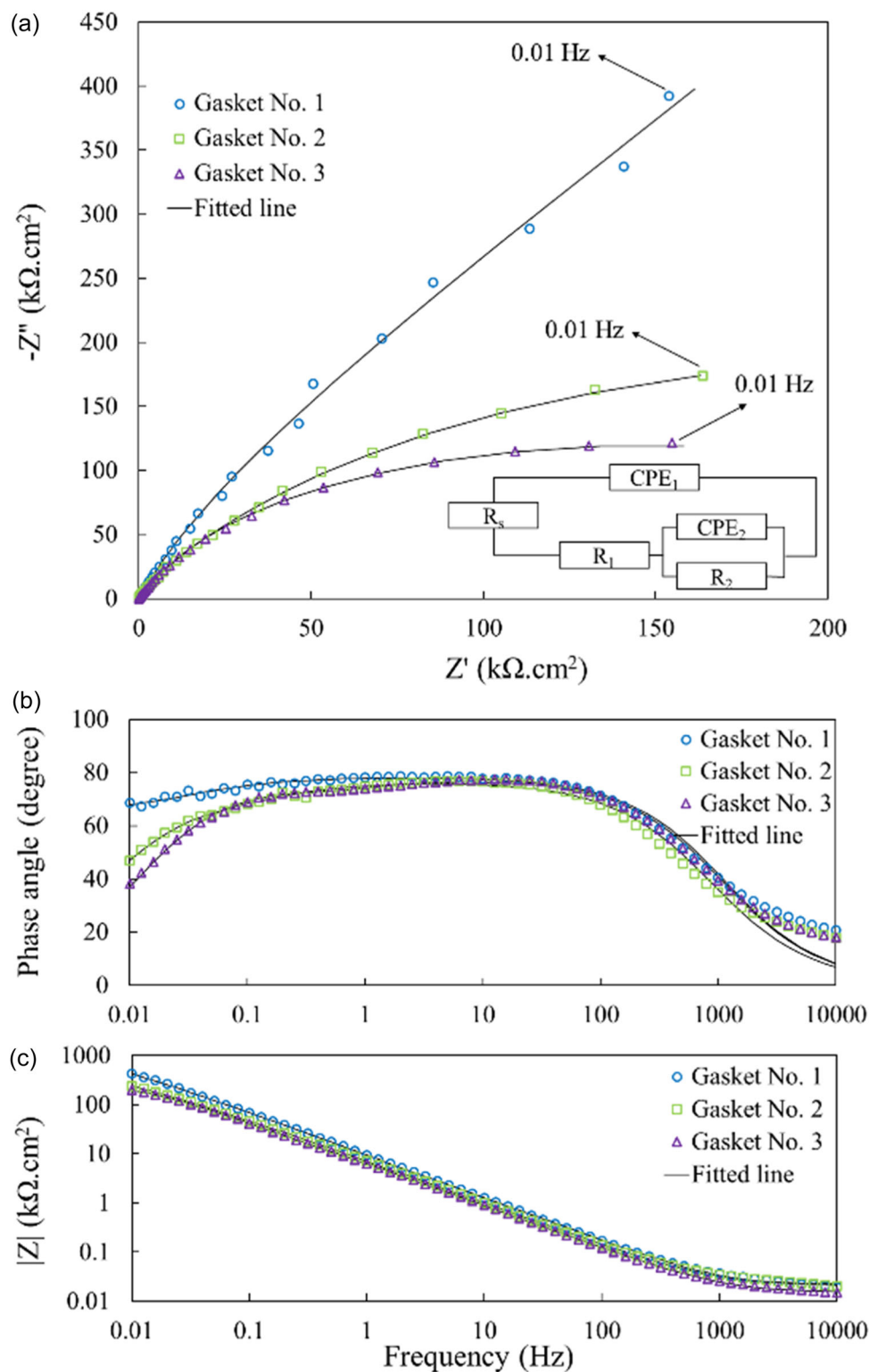


FIGURE 9 (a) Nyquist, (b) Bode phase, and (c) Bode modulus representation of electrochemical impedance response of the 321 SS flange sample plates exposed to the 3.5 wt% NaCl at 50°C under different gap thicknesses. [Color figure can be viewed at [wileyonlinelibrary.com](https://onlinelibrary.wiley.com/terms-and-conditions)]

thickness to 3.17 mm, and it has the minimum value with a gap thickness of 6.35 mm, which demonstrates 293 k $\Omega$  cm $^2$ . The EIS analysis indicates that increasing the gap thickness between two flanges results in an

increase in  $R_{total}$ . Furthermore, it is observed that the value  $R_2$  has a higher contribution compared to  $R_1$ . This observation suggests that the mass transfer of species (such as metal ions or oxygen-containing species)

TABLE 6 Electrochemical parameters estimated by fitting the EEC to the EIS data of 321 SS under various gap thicknesses.

Gasket No.	Gap thickness/g (mm)	$R_s$ ( $\Omega$ )							
		$R_1$ ( $k\Omega\text{ cm}^2$ )	$CPE_1$ ( $\mu\Omega^{-1}\text{ s}^n\text{ cm}^{-2}$ )	$n_1$	$R_2$ ( $k\Omega\text{ cm}^2$ )	$CPE_2$ ( $\mu\Omega^{-1}\text{ s}^n\text{ cm}^{-2}$ )	$n_2$	$R_{\text{total}}$ ( $k\Omega\text{ cm}^2$ )	
1	1.58	2.11	995	21.3	0.87	9730	6.81	0.72	10 725
2	3.17	2.21	224.48	29.28	0.85	257.62	15.77	0.84	482
3	6.35	1.55	85.38	31.31	0.86	207.61	6.98	0.95	293

Abbreviations: EEC, electrical equivalent circuit; EIS, electrochemical impedance spectroscopy.

through the passive layer is slower as the gap thickness decreases.

### 3.4 | Corrosion morphology

Figure 10 presents the crevice corrosion morphologies of a 321 SS flange sample plate after a potentiostatic polarization test for 12 h with Gasket No. 1. The corroded area is located at the interface of the flange and gasket, and the maximum corroded depth is located near the gasket area as shown in the color map of Figure 10a. According to the critical crevice solution theory, the acidification of the crevice is due to the oxygen concentration cell, and  $\text{Cl}^-$  ions that enter the crevice, and as well through the hydrolysis reactions that make the crevice acidic and break down the passive layer. As there is a compressive stress applied on the gasket with 15 MPa, it is difficult for the solution to penetrate through the gasket and flange sample plate interface. Therefore, in the initial steps, corrosion develops through the vertical direction and then it penetrates under the gasket area. As the solution in the crevice is locally acidic, the grain boundaries are observed in the corroded area, which is due to the preferential corrosion of grain boundaries in an acidic solution (Figure 10c). The morphology of the corrosion on the edges of the corroded area is different in the region exposed to the solution (Figure 10b) and in the region under the gasket (Figure 10d). Figure 10b shows that on the side exposed to the solution, there is a sharp edge between the severely corroded area and the passive area, while no crack was observed. However, Figure 10d reveals that the corroded area under the gasket is full of cracks, and these cracks are presented with greater detail in Figure 10e. As the flange-gasket interface is under stress, possibly these cracks are attributed to the effect of the local vertical surface stress<sup>[34]</sup> on the corroded area and coarsening the pits or cracks and lead to the propagation of corrosion in this area. The profile of the corroded area in Figure 10f shows that the corroded depth is the highest in the severely corroded area, and it decreases as corrosion

propagates in the area under the gasket. Comparing the corroded region in the lightly corroded area with other literature that studied crevice corrosion reveals that in those studies, cracks were not observed, as the stress levels were not as high as in this study. Pits without cracks are observed near the crevice-corroded area.<sup>[35,36]</sup>

## 4 | DISCUSSION

### 4.1 | Effect of gap thickness on the flange face corrosion

Crevice corrosion on the SSs in a neutral chloride solution occurs due to the formation of an oxygen concentration cell between the crevice or occluded area and the bulk solution (Figure 11a). Because of the low oxygen concentration in the crevice,  $\text{Cl}^-$  ions react with metal ions ( $\text{M}^+$ ) to maintain the electric balance (Figure 11b).<sup>[16]</sup> Then, hydrolysis will take place, lowering the pH inside the crevice and causing acidification. Consequently, the passive layer in the crevice area transforms into the active area. This transformation causes the potential of the SS sample to drop in the active region due to the  $IR$  drop, where  $I$  refers to the current and  $R$  refers to the resistance.<sup>[37]</sup> Based on the electrochemical results, it can be concluded that the thickness of the crevice gap (shown in Figure 11b) between the flange faces, influenced by the presence of the gasket or flange raised faces, affects the resistance of the flange sample plates to both general and localized corrosion (pitting and crevice).

On the corroded sample plates, a larger crevice-corroded area is observed with a decreasing gap thickness, and deeper pits are observed with an increasing gap thickness. For the sample plate used with Gasket No. 3 in CPP, crevice corrosion is not observed as the gap thickness is wide enough to allow more local fluid circulation. In this case, with the gap thickness at its maximum value, the flowing solution has caused damage to the passive layer. Even at higher

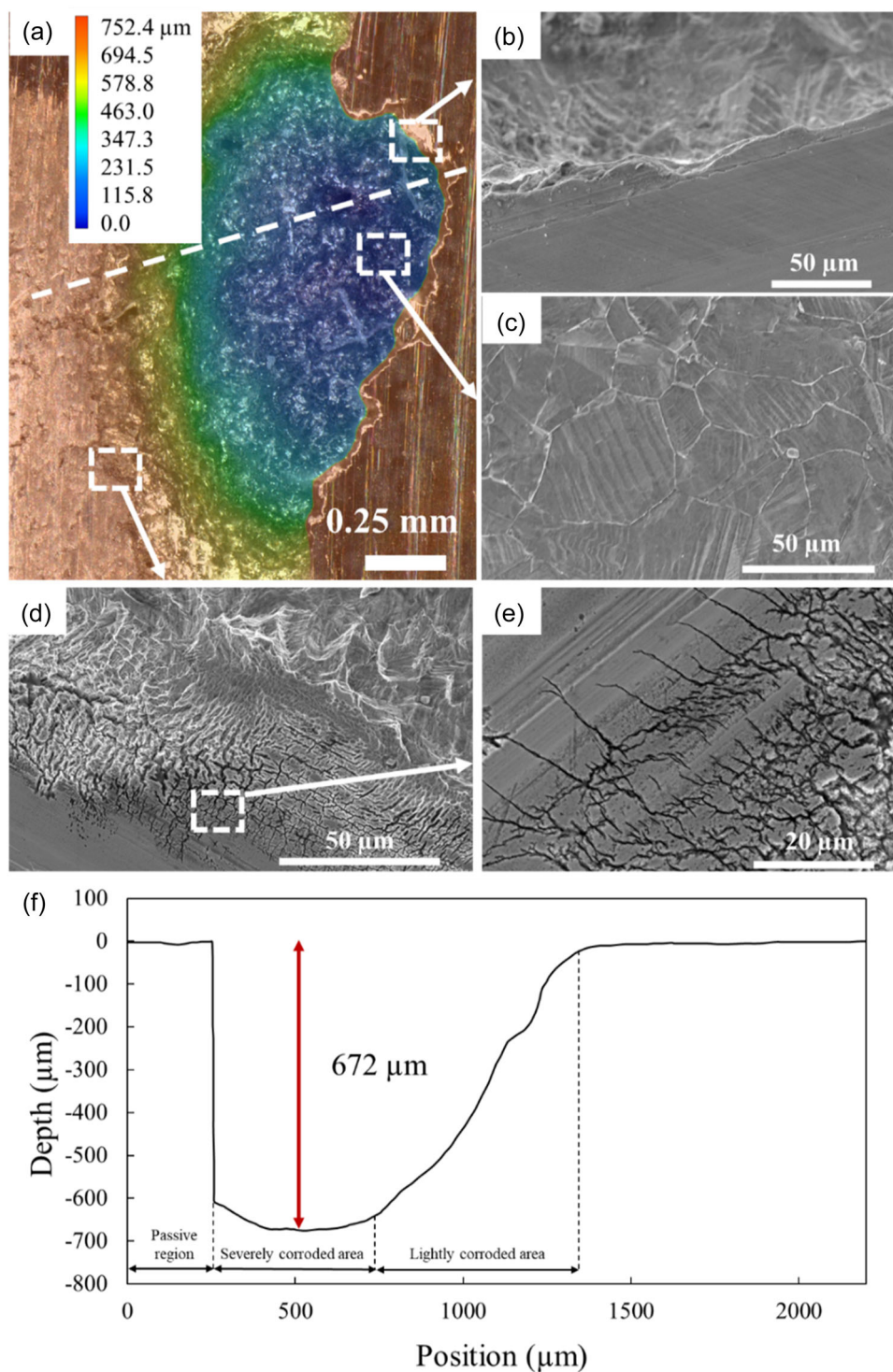


**FIGURE 10** Crevice corrosion morphology of 321 SS flange sample plate tested with Gasket No. 1 after 12 h of potentiostatic polarization in a 3.5 wt% NaCl solution of 50°C. (a) Corroded interface area, (b) severely corroded area and the passive region, (c) severely corroded area, (d) corroded area under the gasket, (e) cracks under the gasket. [Color figure can be viewed at [wileyonlinelibrary.com](https://onlinelibrary.wiley.com)]

potentials, more pits have formed in the area exposed to the solution and have deepened. The earlier initiation of crevice corrosion at the same applied potential on the flange sample plate with Gasket No. 1, along with a higher development current

density, confirms that Gasket No. 1 creates the most susceptible conditions for the initiation and propagation of crevice corrosion.

As the gap thickness increases, it allows more space for the circulating solution in the fixture to enter the gap, and

there is an increase in the volume of the solution within the gap (as shown in Figure 12). This prevents the depletion of oxygen concentration in the crevice (interface of flange and gasket), consequently leading to observed delays in the initiation of crevice corrosion in potentiostatic tests. Additionally, no crevice corrosion is observed in the flange sample plate used with Gasket No. 3 in CPP tests.

The erosion effect of the flowing solution inside the fixture, with the presence of  $\text{Cl}^-$  ions, damages the passive layer formed on the flange sample plate. This damage results in lower resistance observed in the EIS results and an increase in the average pit depth as the gap thickness increases.

The initiation of crevice corrosion can be explained by the potential drop ( $IR$  drop) theory,<sup>[38]</sup> that is, the decrease in potential that occurs within a crevice or gap as a result of the resistance encountered by an electric current passing through the solution in the crevice. This theory states that when the surface of the stainless steel is in the passive form, the  $IR$  drop (derived from Equation 7) causes the crevice area to transition into the active region, initiating crevice corrosion.<sup>[39,40]</sup>

$$IR = \frac{x_{\text{pass}} I}{\sigma w t}, \quad (7)$$

where  $IR$  denotes the potential drop measured in mV,  $x_{\text{pass}}$  stands for the distance from the crevice mouth to the active-passive boundary within the crevice, measured in cm. The

variables include  $I$  for current in mA,  $\sigma$  for conductivity in  $\Omega^{-1} \text{cm}^{-1}$ ,  $w$  for crevice width in cm, and  $t$  for crevice gap thickness in cm. According to Equation (7), the crevice gap, influences the  $IR$  drop and has an inverse relation.

While larger gaps between the flange and gasket may cause more damage to the passive layer and increase the general corrosion rate, the threat of crevice corrosion poses a greater danger to the integrity of an engineering structure. As a localized form of corrosion, it propagates in the confined area between the gasket and flange, rapidly degrading the flange material in a hidden manner. Therefore, it is recommended to use a thicker gasket in bolted flanged joints.

## 4.2 | Effect of crevice depth ( $d$ ) on the flange face corrosion

The variation in crevice depth, denoted as  $d$ , affects the transfer of species between the bulk and crevice solution. When the crevice depth reaches its maximum value of 7.49 mm, the exchange of species between the bulk and crevice solution becomes more challenging. This suggests that, during the crevice corrosion process, oxygen is consumed more rapidly by the cathodic reaction in deeper crevices. Consequently, the acidification process is accelerated, leading to a shorter incubation time for crevice corrosion at a crevice depth of 7.49 mm. For  $d$  values of 3.81 and 0, as the flowing

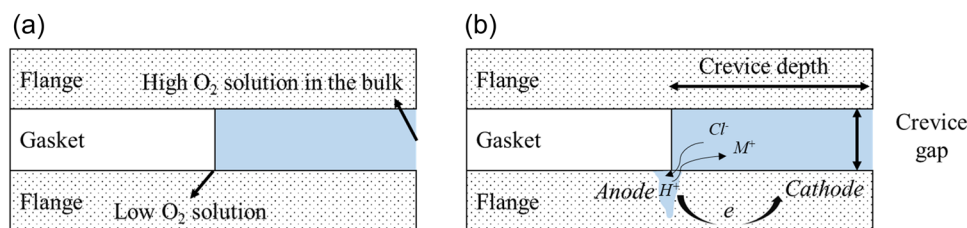


FIGURE 11 Schematic representation of (a) the formation of oxygen concentration cells in the crevice and (b) acidification of the crevice due to hydrolysis. [Color figure can be viewed at [wileyonlinelibrary.com](http://wileyonlinelibrary.com)]

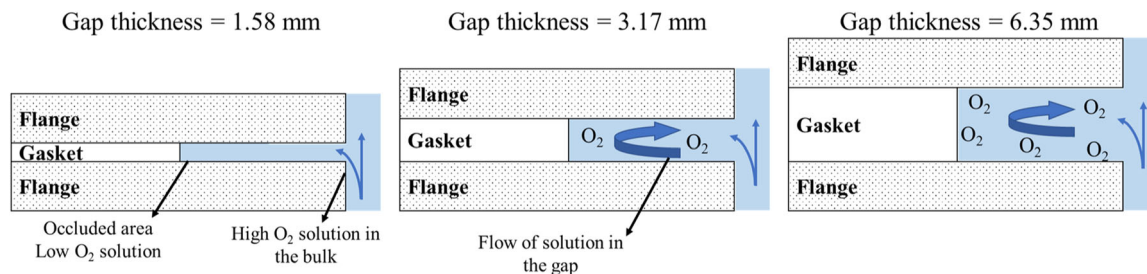


FIGURE 12 Schematic representation of the effect of gap thickness on the flow of solution in the gap between two flanges and the volume of the solution. [Color figure can be viewed at [wileyonlinelibrary.com](http://wileyonlinelibrary.com)]

solution passes, it avoids the formation of stagnant solution in the interface of the flange and gasket, preventing acidification and breakdown of the passive layer.

Equation (7) also illustrates the influence of crevice depth on crevice corrosion. As mentioned in Section 4.1,  $x_{\text{pass}}$  is the distance between the crevice mouth and the active-passive boundary inside the crevice, and in this study, we can substitute the  $x_{\text{pass}}$  value with  $d$  (crevice depth as shown in Figure 11b). Thus, it can be concluded that for  $d = 3.81$  and  $0$  mm, the  $IR$  drop remains in the passive region, preventing the initiation of crevice corrosion.

However, in the CPP tests, due to the formation of pits at high potentials on the exposed area ( $d = 3.81$  mm), the  $IR$  drop increases significantly as the current  $I$  increases with the formation of pits on the flange face. Therefore, crevice corrosion also occurred in the interface of the flange and gasket. Full-face gaskets protect the flange surface from pitting and general corrosion; therefore, it is recommended to use these types of gaskets in bolted flanged joints.

## 5 | CONCLUSION

In the present study, the effect of gap size (thickness and depth) on the 321 SS flange surface corrosion was studied using electrochemical techniques and surface analysis methods. All electrochemical tests were performed with a fixture that simulates the real-world conditions in bolted flanged joints including the applied stress on the gasket, fluid flow inside the fixture, and the crevice geometry between the gasket and flange. Both general and localized corrosion of the flange sample plates are investigated in this study. It is found that gaps between the flange plates in bolted flanged joints will cause localized corrosion on the flange surfaces. In this study, gaskets are used to create the gaps, as they are commonly used in various applications such as wind turbines and pipe flanges. The findings of this study are as follows:

- The passive potential range  $|E_{\text{corr}} - E_b|$  decreases as the volume of the gap increases, and both crevice corrosion and pitting corrosion cause the breakdown of the passive layer in CPP tests. The gap size influences the contribution of crevice corrosion and pitting corrosion on the flange surface.
- Both EIS and CPP tests reveal that the overall corrosion resistance of the flange surface is influenced by variations in the gap size. With an increase in gap thickness, the corrosion rate of the flange surface rises. Additionally,

reducing the  $d$  value (or crevice depth) leads to a decrease in the general corrosion rate of the flange surfaces.

- Corrosion pits develop on the area exposed to the solution, and the average pit depth increases with the widening of the gap thickness. In contrast, the average pit depth decreases as the value of  $d$  decreases and the surface is covered with the gasket.
- Crevice corrosion initiates at the flange gasket interface and propagates to the area under the gasket. The initiation time of crevice corrosion increases with an increase in gap thickness. No crevice corrosion is observed on sample plates with the same ID as the gasket.

## AUTHOR CONTRIBUTIONS

**Soroosh Hakimian:** Conceptualization; methodology; investigation; formal analysis; software; writing—original draft. **Abdel-Hakim Bouzid:** Project administration; methodology; resources; supervision; writing—review and editing. **Lucas A. Hof:** Project administration; methodology; resources; supervision; writing—review and editing.

## ACKNOWLEDGMENTS

This work was supported by the Natural Sciences and Engineering Research Council of Canada (NSERC) under the Discovery Grant (RGPIN-2019-05973 and RGPIN-2021-03780).

## DATA AVAILABILITY STATEMENT

The data that support the findings of this study are available from the corresponding author upon reasonable request.

## ORCID

Soroosh Hakimian  <http://orcid.org/0009-0000-4944-9931>

## REFERENCES

- [1] N. R. Nelson, N. S. Prasad, A. S. Sekhar, *Int. J. Press. Vessels Pip.* **2023**, *204*, 104975.
- [2] S. Z. Li, H. Li, X. H. Zhou, Y. H. Wang, X. H. Li, D. Gan, R. H. Zhu, *J. Civ. Struct. Health Monit.* **2023**, *13*, 67.
- [3] A. Nechache, A. H. Bouzid, *Int. J. Press. Vessels Pip.* **2007**, *84*, 185.
- [4] W. Weijtjens, A. Stang, C. Devriendt, P. Schaumann, *J. Constr. Steel Res.* **2021**, *176*, 106361.
- [5] M. B. Lachowicz, M. M. Lachowicz, *Materials* **2021**, *14*, 1485.
- [6] J. Zhang, J. Heng, Y. Dong, C. Baniotopoulos, Q. Yang, *Eng. Struct.* **2024**, *301*, 117309.
- [7] A. Mehmanparast, S. Lotfian, S. P. Vipin, *Metals* **2020**, *10*, 732.
- [8] S. Hakimian, A.-H. Bouzid, L. A. Hof, *J. Adv. Join. Process.* **2024**, *9*, 100200.
- [9] S. Bond, A. Lattimer, P. Welsford, *Corros. Prev.* **2018**, *2018*.
- [10] A. Nechache, A. H. Bouzid, *Int. J. Press. Vessels Pip.* **2008**, *85*, 486.
- [11] A. Bouzid, A. Chaaban, A. Bazergui, *J. Press. Vessel Technol.* **1995**, *117*, 71.

- [12] A. Bouzid, A. Chaaban, A. Bazergui, *Can. Soc. Mech. Eng.* **1994**, *21*, 415.
- [13] A. H. Bouzid, M. Derenne, M. El-Rich, Y. Birembaut, *Weld. Res. Counc. Bull.* **2004**, *496*, 1.
- [14] K. Worden, *Fuels and Petrochemicals Division 2014—Core Programming Area at the 2014 AIChE Spring Meeting and 10th Global Congress on Process Safety*, 2014, *2*, 1000.
- [15] E. M. Costa, B. A. Dedavid, C. A. Santos, N. F. Lopes, C. Fraccaro, T. Pagartanidis, L. P. Lovatto, *Eng. Fail. Anal.* **2023**, *144*, 106955.
- [16] Q. Hu, G. Zhang, Y. Qiu, X. Guo, *Corros. Sci.* **2011**, *53*, 4065.
- [17] B. Luo, Q. Hu, J. Liu, F. Huang, *J. Mater. Res. Technol.* **2022**, *21*, 2584.
- [18] E. Shojaei, M. Mirjalili, M. H. Moayed, *Corros. Sci.* **2019**, *156*, 96.
- [19] S. Hakimian, A. H. Bouzid, L. A. Hof, *J. Press. Vessel Technol. Trans. ASME* **2024**, *146*, 11302.
- [20] L. Marchand, M. Derenne, A. Bazergui, *J. Press. Vessel Technol.* **1992**, *114*, 1.
- [21] L. Marchand, A. Bazergui, M. Derenne, B.S. Nau (Eds:) *Fluid Sealing*, Springer, Netherlands, Dordrecht **1992**, p. 209.
- [22] ASTM G61, Standard Test Method for Conducting Cyclic Potentiodynamic Polarization Measurements for Localized Corrosion Susceptibility of Iron-, Nickel-, or Cobalt-Based Alloys, West Conshohocken **2018**.
- [23] ASTM G102-89, Standard Practice for Calculation of Corrosion Rates and Related Information from Electrochemical Measurements **2015**.
- [24] ASTM G1, Standard Practice for Preparing, Cleaning, and Evaluating Corrosion Test Specimens, West Conshohocken **2017**.
- [25] J. Schindelin, I. Arganda-Carreras, E. Frise, V. Kaynig, M. Longair, T. Pietzsch, S. Preibisch, C. Rueden, S. Saalfeld, B. Schmid, J. Y. Tinevez, D. J. White, V. Hartenstein, K. Eliceiri, P. Tomancak, A. Cardona, *Nat. Methods* **2012**, *9*, 676.
- [26] B. Cai, Y. Liu, X. Tian, F. Wang, H. Li, R. Ji, *Corros. Sci.* **2010**, *52*, 3235.
- [27] E. Vasilescu, P. Drob, D. Raducanu, I. Cinca, D. Mareci, J. M. Calderon Moreno, M. Popa, C. Vasilescu, J. C. Mirza Rosca, *Corros. Sci.* **2009**, *51*, 2885.
- [28] S. H. Salleh, S. Thomas, J. A. Yuwono, K. Venkatesan, N. Birbilis, *Electrochim. Acta* **2015**, *161*, 144.
- [29] X. Liu, Y. Sui, H. Zhang, Y. Liu, X. Li, J. Hou, *Mater. Corros.* **2024**. <https://doi.org/10.1002/maco.202414280>
- [30] S. Esmailzadeh, M. Aliofkhaezai, H. Sarlak, *Prot. Met. Phys. Chem. Surf.* **2018**, *54*, 976.
- [31] X. He, D. S. Dunn, A. A. Csontos, *Electrochim. Acta* **2007**, *52*, 7556.
- [32] M. Nishimoto, J. Ogawa, I. Muto, Y. Sugawara, N. Hara, *Corros. Sci.* **2016**, *106*, 298.
- [33] S. Habibzadeh, L. Li, D. Shum-Tim, E. C. Davis, S. Omanovic, *Corros. Sci.* **2014**, *87*, 89.
- [34] C. Fischer, H. Zitter, *Mater. Corros.* **1960**, *11*, 17.
- [35] E. Hornus, K. Wang, M. Pabbruwe, A. Kop, C. Jones, A. Salleh, M. Salasi, M. Iannuzzi, *Corros. Sci.* **2021**, *190*, 109704.
- [36] B. Malki, G. Berthomé, T. Souier, C. Boissy, I. Guillotte, B. Baroux, *J. Electrochem. Soc.* **2021**, *168*, 101504.
- [37] H. W. Pickering, *Corros. Sci.* **1989**, *29*, 325.
- [38] G. F. Kennell, R. W. Evitts, K. L. Heppner, *Corros. Sci.* **2008**, *50*, 1716.
- [39] R. S. Lillard, J. R. Scully, *J. Electrochem. Soc.* **1994**, *141*, 3006.
- [40] M. I. Abdulsalam, *Mater. Corros.* **2007**, *58*, 511.

**How to cite this article:** S. Hakimian, A.-H. Bouzid, L. A. Hof, *Mater. Corros.* **2024**, 1–18. <https://doi.org/10.1002/maco.202414367>